

Experimental estimation and control of natural Tollmien-Schlichting waves

H. J. Tol[†], M. Kotsonis and C. C. de Visser

Faculty of Aerospace Engineering, Delft University of Technology, Postbus 5058, 2600GB
Delft, The Netherlands

(Received xx; revised xx; accepted xx)

A compensator strategy that incorporates a physics-based model has been applied to an experimental laminar boundary layer flow to suppress Tollmien-Schlichting waves naturally occurring in low-free stream turbulence conditions. Experiments have been conducted on a flat plate with a strong adverse pressure gradient. A Kalman filter is used to estimate the effect of upstream disturbances based on pressure information from a single microphone embedded in a cavity within the body of the plate. This information is used to cancel the perturbations using a surface DBD plasma actuator. The estimates obtained from the Kalman filter are compared with experimental data obtained with PIV. It is shown that the Kalman filter is able to estimate the spatio-temporal behaviour of the perturbation field even though it relies on a-priori assumptions on the upstream disturbance environment. The performance of the controller and the robustness to varying freestream velocities is analysed in comparison with open-loop continuous forcing. It is shown that the controller is able to additionally reduce the power at the most amplified frequencies with more than one order of magnitude and is capable of reducing the standard deviation of the downstream sensor signal between 40-60% for a range of off-design free-stream velocities.

1. Introduction

Tollmien-Schlichting (TS)-waves are the main reason for transition on unswept wings in low free-stream turbulence conditions ($< 1\%$). By suppressing the growth of TS-waves in their early linear stage it may be possible to delay the transition process and to reduce skin friction drag. The benefits of applying linear model-based control for transition delay have been demonstrated in both numerical studies and experiments (Kurz *et al.* 2013; Juillet *et al.* 2014; Gautier & Aider 2014; Goldin *et al.* 2013; Fabbiane *et al.* 2015). Boundary layers behave as noise amplifiers of upstream disturbances and are in particular challenging to control. They are highly receptive to disturbances and there exist only a small window in time to suppress convective instabilities. TS-waves appear in distinct wavepackets which are generally uncorrelated to each other. The convective nature of the flow and the lack of a physical downstream to upstream feedback mechanism favour a feedforward actuator-sensor configuration. In this case a sensor upstream of the actuator measures the incoming perturbations, and the controller can use a model of the perturbation evolution to devise an actuator input that cancels the perturbations. It is well known that such disturbance feedforward systems rely on an accurate model of the flow, including an accurate representation of the upstream disturbance environment (Fabbiane *et al.* 2015; Sipp & Schmid 2016).

The model can be obtained either from the governing equations or from a sample of

[†] Email address for correspondence: h.j.tol@tudelft.nl

input-output measurements using systems identification techniques. Numerical studies commonly focus on optimal and robust estimation and control laws based on a Galerkin state-space formulation of the linearised Navier-Stokes equations (Bewley & Liu 1998; Bagheri *et al.* 2009). Such white/physics model-based controllers provide important physical insights and give the best possible (optimal) performance for a given set of inputs-outputs. However, it requires the use of empirical model reduction methods (Rowley & Dawson 2017) to synthesise experimentally feasible controllers. Furthermore, this approach requires a-priori assumptions on the source and distribution of the external disturbances, which is not precisely known in real environments. Hervé *et al.* (2012) and Sipp & Schmid (2016) argued that Galerkin models are inappropriate due to their difficulty in obtaining an accurate representation of the upstream disturbance environment. To mitigate these challenges, they recommended data-based system identification techniques for experimental control of amplifier flows. In this case the input-output relation is directly identified from a sample of input-output measurements. This approach avoids the need for a-prior disturbance models by processing information from an upstream sensor, which approximates the influence of the upstream disturbances. For example, by incorporating this information in an auto-regressive design (Gautier & Aider 2014) or finite impulse response filters (Juillet *et al.* 2014). A drawback on the other hand is that system-identified linear models can present challenges when nonlinearities and statistical velocity components are present in the flow.

This work investigates the practical feasibility and performance of physics-model based compensators for estimation and control of Tollmien-Schlichting waves. Of the previous works, the experimental setup and the control approach taken in this study mostly resembles the work of Fabbiane *et al.* (2015). Fabbiane *et al.* (2015) were the first to demonstrate the suppression of artificially induced perturbations in experiments based on a white DNS model of the flow. To the best of our knowledge this the first study on physics-based control of natural flow perturbations, bringing it closer to non-academic applications. Recently, Tol *et al.* (2017) introduced a new framework to synthesize reduce controllers directly from the governing equations without the use of prior numerical data or empirical model reduction. It was shown that the use of physically motivated inflow disturbance models allows for efficient estimation of the perturbations, also in the case of unknown/unmodelled upstream disturbances. This framework is applied in this study for estimation and control of Tollmien-Schlichting waves naturally occurring in low-free stream turbulence conditions. The objective of this study is twofold. The first objective is to investigate if state-estimators are able to estimate the spatio-temporal behaviour of natural perturbations. State estimation is a dual problem to that of controlling the flow and relies on a-priori assumptions of the disturbance characteristics. The spatio-temporal estimates obtained from a Kalman filter are, for the first time, compared with experimental data obtained from PIV. The second objective is to assess the performance of the combined estimation/feedforward control approach.

2. Experimental setup and flow configuration

A schematic of the experimental setup for investigation and control of natural instabilities in a flat boundary layer is shown in figure 1. The experiment is performed in an open-loop wind tunnel with a square cross-section of $0.5 \text{ m} \times 0.5 \text{ m}$ and a free-stream turbulence intensity under 0.2%. Inside the test-section is a flat plate of 1 m long with an elliptical leading edge and a movable flap at the trailing edge to control the stagnation point, which ensures a smooth development of the boundary layer. The freestream velocity is measured with a pitot-static tube located upstream of the leading

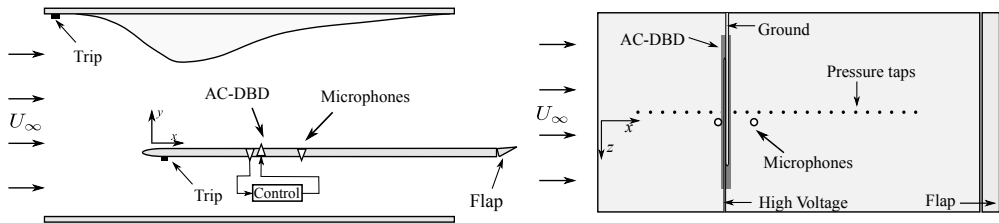
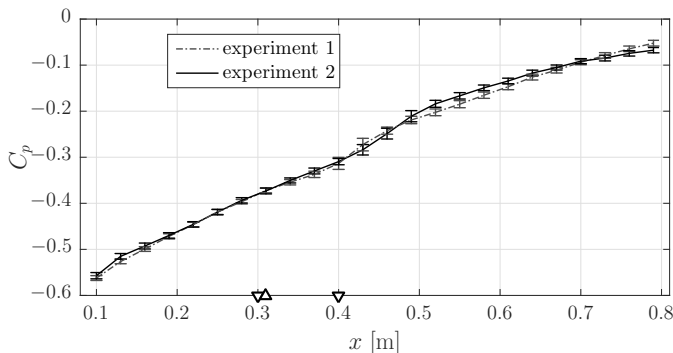


Figure 1: Schematic of the experimental set-up.


 Figure 2: C_p distribution for the two experimental campaigns. The triangles indicate the position of the microphones (∇) and the plasma actuator (Δ).

edge and is set at $U_0 = 9.4$ m/s. Natural perturbations are introduced at the leading edge due to the boundary layer receptivity to acoustic and vortical disturbances and amplify as they convect downstream. An adjustable flexible wall on the roof controls to pressure gradient to increase the amplification rate of the perturbations and to promote transition at the relative low freestream velocities. A streamwise array of 24 pressure taps is used to determine the pressure distribution (C_p) and to characterize the mean flow (see next section). The taps have a uniform spacing of 30 mm with the first tap located at $x = 0.1$ m. Two independent experimental campaigns have been performed. The first study was performed using the setup in figure 1, in an uncontrolled setting, that is without the actuator. The primary objective was to characterize the stability properties crucial for control design and to validate the modelling methodology for dynamic flow estimation. For this experiment PIV was used to compare the estimated perturbation fields with the experimental perturbation fields. These results are presented in section 3 as part of the control design methodology. The objective of the second experiment was show attenuation of the perturbations by means of control, which is presented in section 4. The C_p distribution with the 2σ bounds for both experiments are shown in figure 2. It can be observed that the distributions match closely in the actuator-sensor region up to $x = 0.4$ mm. The step increase in pressure and standard deviation after $x = 0.4$ m indicates transition of the boundary layer.

2.1. Control system elements

The flow is controlled using an alternating current surface dielectric barrier discharge actuator. It consists of a 10 mm wide grounded lower copper electrode of $30\mu\text{m}$ thickness and a 5 mm wide upper electrode connected to a high voltage source. No horizontal gap

was formed between the electrodes and the center of the two electrodes is chosen as the reference position of the actuator, which is placed at $x_{\text{act}} = 0.31$ m. The actuator has a length of 0.3 m in the spanwise direction. Two dielectric layers of polyimide Kapton tape with a total thickness of approximately 100 μm separated the two electrodes. It was verified that the intrusion of actuator has no influence on the transition process. It is driven by a digitally controlled high voltage amplifier. The carrier frequency of the actuator is set to 2 kHz, which is one order of magnitude higher than the most unstable TS-waves for the investigated conditions. For this actuator an operating range from 6 kV_{pp} to 16 kV_{pp} has to be maintained in order to produce a stable discharge. To account for the threshold a mean forcing is applied (Dadfar *et al.* 2013; Fabbiane *et al.* 2015; Kurz *et al.* 2013), whereas the compensator can modulate the amplitude of the high-voltage supply through the control signal ϕ . The compensator will be discussed in detail in section 3. A mean voltage supply of $V_0 = 8\text{kV}_{\text{pp}}$ and $V_0 = 9\text{kV}_{\text{pp}}$ are investigated in this study. The applied voltage signal to the actuator is thus given by $V_{\text{app}} = 0.5(V_0 + \phi) \sin(2\pi f_{\text{act}}t)$ where ϕ is supplied by the compensator. Two M51 microphones were employed to measure the fluctuation pressure at the wall. One microphone located at $x = 0.3$ m provides the compensator with the required feedforward information. Additionally, a second microphone is placed at $x = 0.4$ m to monitor the performance of the compensator. The microphones are embedded in a shielded cavity, within the body of the plate connected to the surface through a small pinhole of 0.1 mm in diameter. The cavity shields the microphone from electromagnetic interferences of the actuator. The sensors are calibrated using a pistonphone to provide the information in Pascals. Labview software controls the input-output logic, processes the measurement data from the microphone and generates the control input to the voltage generator. The control logic runs on a field-programmable gate array (FPGA) inside a CompactRIO device from National Instruments. It consist of three parallel loops. The first loop filters the measurement information using a second order bandpass filter (50-800 Hz) and executes at a sampling frequency of 100 kHz. The bandpass filter filters the DC component, the low frequency background noise and the high frequency noise of the plasma actuator. The second loop contains the compensator which specifies the amplitude modulation of the applied voltage signal and executes at 20 kHz. The third loop executes 100 kHz and generates the signal to the voltage generator.

2.2. Base flow and stability

The base flow is obtained as steady numerical solution of the boundary layer equations. The external free stream boundary condition is matched with the external inviscid velocity obtained from the C_p distributions, $U_e = U_\infty \sqrt{1 - C_p}$. To obtain a sufficiently smooth profile, the inviscid velocity is fitted with a second order polynomial using the C_p data up to $x = 0.4$ m just before the transition location, which is illustrated in Figure 3(a). It should be noted that the local external velocity has increased compared to the freestream velocity because of the favourable pressure gradient imposed by the flexible wall upstream of the plate. A local Falkner-Skan inflow profile $U_e(x) \propto x^m$ is assumed at the location of the first pressure tap $x_0 = 0.1$ m where m is calculated from the inviscid profile $m = (x_0/U_e)(dU_e/dx) = -0.032$. Figure 3(b) shows the local velocity profiles at three locations in the domain. It can be observed that mean flow fits the experimental data well, except near the wall were PIV becomes less accurate. It should be noted that PIV data has only been used for validation purposes and has not been used for computing the base flow.

The two-dimensional linear stability theory (LST) calculations for the base flow are shown in figure 4(a) and the power spectral density (PSD) for the natural perturbations measured by the two pressure sensors is shown in figure 4(b). Based on the empirical

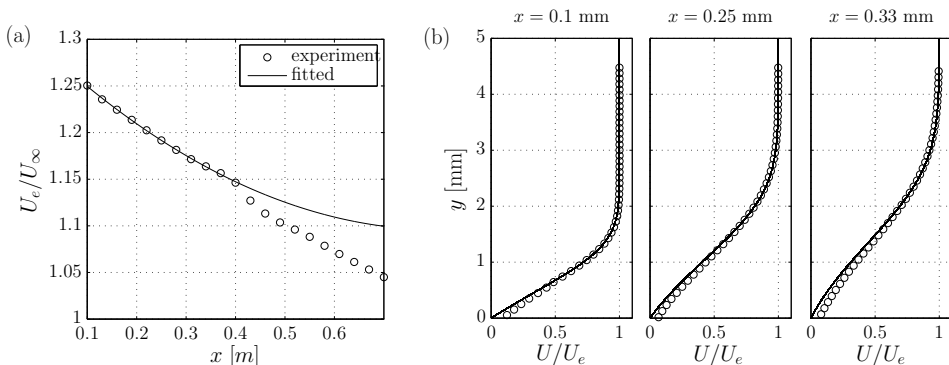


Figure 3: (a) The inviscid external velocity obtained from the static pressure taps and the fit obtained with a second order polynomial using the data up $x = 0.4$ m. (b) Comparison of the computed base flow with experimental data.

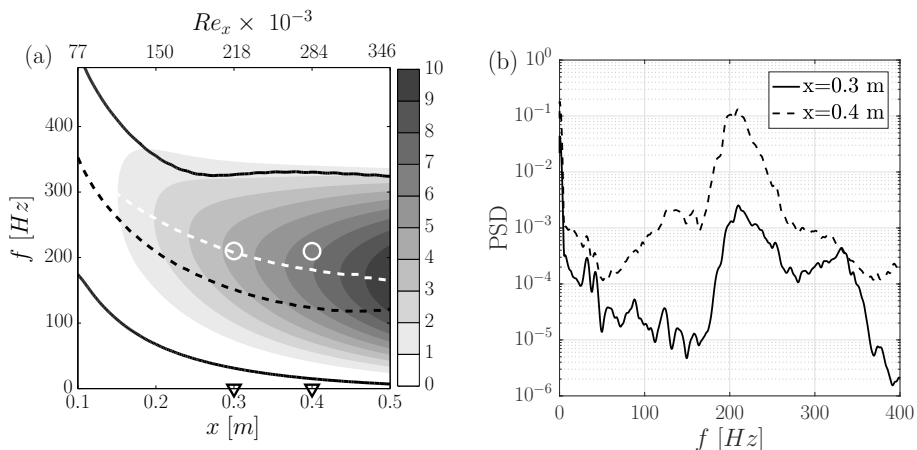


Figure 4: Neutral stability curve (black solid line) and integrated amplification (N) factor contours. The dashed black line shows the local most unstable frequency and the dashed white line shows the local maximum N -factor. The circles indicate the most amplified frequency measured by the pressure sensors.

N -factor method (Van Ingen 2008), LST predicts the location of transition at $x = 0.47$ m where the integrated amplification factor reaches $N \approx 9$. This is close to location at $x = 0.43$ as observed from the C_p measurements in figure 2. The most amplified frequency measured as $x = 0.3$ m is 210 Hz which closely matches the LST predictions (dashed white line). The peak at 330Hz can be contributed by the noise of the windtunnel power supply. The power at 210 Hz increases with two orders of magnitude between $x = 0.3$ m and $x = 0.4$ m. In this region nonlinear effects are also present which explains the mismatch with the LST prediction of the most amplified frequency at $x = 0.4$ m. The good agreement between the theoretical predictions and the experimental results in the actuator/sensor region indicates that linear control based on a 2-D model of the flow can be effective for this setup.

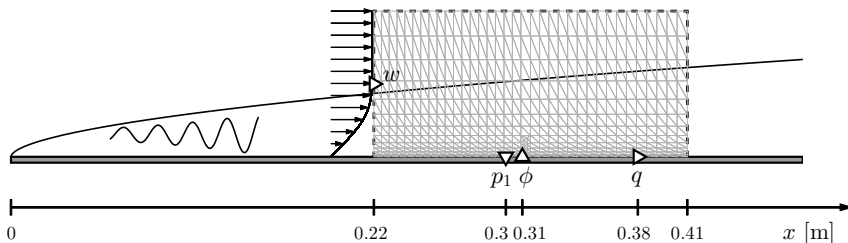


Figure 5: Computational domain, mesh used for the discretisation, and input-output configuration used for control design. The computational domain extends $169\delta_0^*$ in streamwise direction and $18\delta_0^*$ in the wall-normal direction, with $\delta_0 = 1.1$ mm. Measurement p_1 , plasma actuator ϕ , controlled output q and inflow disturbance w .

3. The linear compensator

A disturbance feedforward controller is designed using the framework from Tol *et al.* (2017). The synthesis approach combines state-space discretization of the governing equations using spline elements (Tol *et al.* 2016) with balanced truncation (Moore 1981) to synthesise low order controllers. The computational domain and input-output layout used for control design is shown in figure 5. A localised computational domain $x_c \in [0.22 \text{ m}, 0.41 \text{ m}]$ is considered to avoid very large systems. The local Reynolds number at the beginning of the domain is $Re = U_0\delta_0/\nu = 838$ with $U_0 = 11.3$ m/s and $\delta_0 = 1.1$ mm. The height of the domain is set to $H = 20$ mm $\approx 18\delta_0$. The finite dimensional approximation of the system in state-space format is obtained using Galerkin projection of the linearised Navier-Stokes equations (LNSE) around the base flow with fifth order bivariate spline elements (Lai & Schumaker 2007). This system is in turn used to synthesise the reduced order compensator. This gives rise to the following two systems

$$\dot{\mathbf{u}} = \mathbf{A}\mathbf{u} + \mathbf{B}_1\mathbf{w} + \frac{1}{k}\mathbf{B}_2\phi, \quad p_1 = \mathbf{C}\mathbf{u} + \mathcal{D}w \quad (3.1)$$

$$\left. \begin{aligned} \hat{\mathbf{u}}_r &= \mathbf{A}\hat{\mathbf{u}}_r + \mathbf{B}_2\tilde{\phi} + \mathbf{L}(p_1 - \hat{p}_1), & \hat{p}_1 &= \mathbf{C}\hat{\mathbf{u}}_r \\ \tilde{\phi} &= \frac{1}{k}\phi = -\mathbf{F}\hat{\mathbf{u}}_r \end{aligned} \right\} \quad (3.2)$$

Equation (3.1) is the full order system with $(\mathbf{A}, \mathbf{B}, \mathbf{C}, \mathcal{D})$ the state-space matrices resulting from the discretisation, \mathbf{u} the full order state vector, ϕ the control input that specifies the amplitude modulation of the actuator voltage signal, p_1 the upstream sensor signal and $\mathbf{w} = (w_d, w_n)$ the vector of state disturbances and measurement noise to account for uncertainties in the control design. The role of the gain k , and the underlying continuous models of the actuator \mathbf{B}_2 , sensor \mathbf{C} and the external disturbances \mathbf{B}_1 will follow later in this section. System (3.1) is balanced and reduced to retain the r most controllable/observable modes in the reduced order model (ROM) defined by $(\mathbf{A}, \mathbf{B}, \mathbf{C}, \mathcal{D})$. Based on the available memory on the FPGA the order of the ROM was set to $r = 40$. The ROM is subsequent used to design the compensator defined by (3.2) with \mathbf{L} and \mathbf{F} respectively the estimator (Kalman) gain and state-feedback gain to be optimized. The compensator combines a Kalman filter, which constructs a low-dimensional approximation from the upstream measurements p_1 and a state feedback, which computes the control signal ϕ from the estimated state. An LQG design is employed

to synthesise the compensator by solving two independent optimization problems based on the ROM (Zhou *et al.* 1996, Chapter 14). First the state-estimator is discussed.

3.1. State estimator

The Kalman filter is designed to minimize the covariance of the difference between the reduced order state \mathbf{u}_r and the estimate state $\hat{\mathbf{u}}_r$ assuming that the system is excited by Gaussian white noise. This requires a-priori assumptions on the source and distribution of the upstream disturbance environment modelled by \mathcal{B}_1 and an output equation which relates the upstream perturbations with the pressure fluctuations at the measurement location at the wall. The derivation of the output equation is not trivial as the pressure is initially eliminated by formulating the LNSE on a divergence free state-space to avoid singularities. In Tol *et al.* (2018) a novel method is presented to retrieve the output equation based on spatial integration of LNSE along the inflow and wall boundaries in a separate step independently of the derivation of the state equations. Mathematically, the output operator \mathcal{C} represents the formal inverse of the pressure gradient along the inflow and wall boundaries. The disturbance model forms the basis for the model reduction and is crucial to allow an accurate reduction of the dynamics and capturing the relevant flow physics. When model reduction is used in the design of the compensator, the spatio-temporal dynamics which are retained in the ROM and can be estimated depend on the spatio-temporal dynamics that are excited by the external disturbance model. It is shown in Tol *et al.* (2017), through a spatio-temporal frequency response analysis, that the use of inflow disturbance models allows for efficient estimation of the dominant flow perturbations in broad temporal frequency bandwidth. The external disturbance model assumes stochastic excitation of the most amplified Orr-Sommerfeld eigenfunction. For the investigated conditions, the most amplified eigenfunction at the inflow $x = 0.22$ m is found at $f = 240$ Hz, see also figure 4. It should be noted that in case of stochastic excitation the eigenfunction is excited over all temporal frequencies. Also at other frequencies than the design frequency, the inflow perturbation will develop spatially to modal perturbations with different wavelengths and growth rates. As a result the single mode disturbance model also allows for estimation of multiple frequency wavepackets Tol *et al.* (2017).

To gain physical insights in the estimator performance and for validation of the modelling methodology the estimates obtained from the estimator are compared with experimental data obtained from PIV. For this an uncontrolled experiment was performed in which the timestamps of the PIV snapshots were synchronised with a sample of pressure measurements. In total 500 PIV snapshots were obtained sampled at a rate of 2.2 Hz. The upstream sensor signal p_1 was used as input to the estimator

$$\hat{\mathbf{u}}_r = \mathbf{A}\hat{\mathbf{u}}_r + \mathbf{L}(p_1 - \mathbf{C}\hat{\mathbf{u}}_r), \quad \hat{\mathbf{u}}_r(0) = 0, \quad (3.3)$$

which filters the data and reconstruct the state \mathbf{u}_r in the process. The state \mathbf{u}_r is the vector of reduced order expansion coefficients, which is related to the full order coefficients through $\mathbf{u} = \mathbf{S}_r^{-1}\mathbf{u}_r$, where \mathbf{S}_r^{-1} are the first r columns of the inverse of the similarity transformation $\mathbf{u} \mapsto \mathbf{S}\mathbf{u}$ used to balance the system required for model reduction. In this way the flow field could be reconstructed from the reduced order estimates and compared with experimental data at the PIV timestamps. A POD reconstruction of the PIV data was necessary in order to measure TS-waves in the control region, since the measurement noise overlays the TS-waves that have a low amplitude. The PIV data was reconstructed in the domain $x \in [0.285 \text{ m}, 0.345 \text{ m}]$, which encapsulates the actuator/sensor used for control, using the first seven POD modes which capture 30% of the total energy. It was

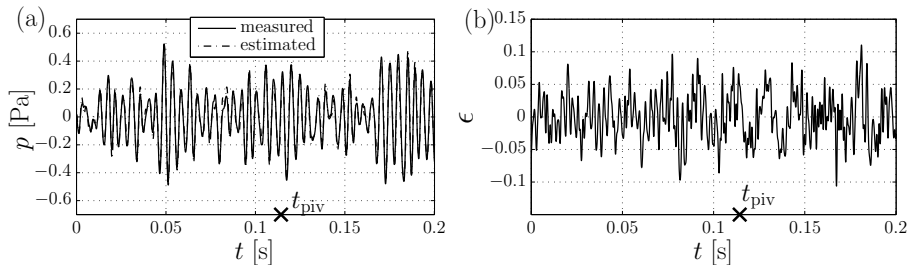


Figure 6: Filtering of the upstream sensor signal. (a) The measured pressure and estimated pressure. (b) the estimation error

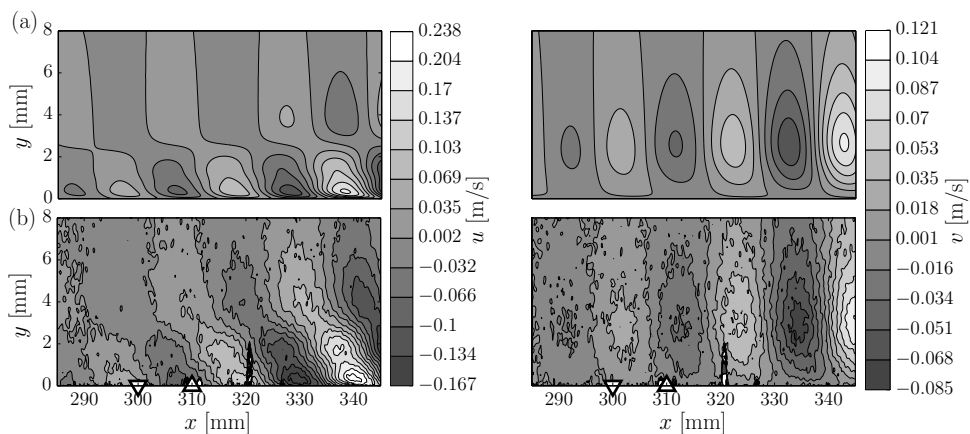


Figure 7: Snapshot of the perturbation velocity in the control region. (a) Estimated velocity field. (b) Instantaneous POD reconstructed snapshot. The triangles indicate the position of the microphone (∇) and the plasma actuator (Δ).

verified that the inclusion of more modes was only adding more uniform noise to the reconstruction.

Figure 6 illustrates the filtering of the pressure measurements for a sample of 0.2 s and figure 7 shows the instantaneous estimated field and instantaneous POD reconstructed field at $t = t_{\text{piv}}$. Similar results were obtained for other timestamps were the TS-waves were of sufficient amplitude. Figure 8 shows the root-mean-square (rms) value of the estimated and measured streamwise and wall normal velocity components at four different streamwise locations. It should be noted that this is a temporal statistical quantity, while the PIV data is not time-resolved. Furthermore, the PIV data is less accurate near the wall and more noisy upstream, where the TS-waves have a lower amplitude. Nonetheless important observations can be made from these results. The Kalman filter is able to reconstruct the signal and to obtain spatial-temporal estimates of the perturbation field. Both the shape, magnitude and phase of the perturbations match well in particular for the wall-normal component. The wall-normal component also has a simpler spatial structure and is less pronounced at the wall allowing for a better reconstruction with POD. The most disagreement between the measured and reconstruct signal as well as between the measured and reconstructed perturbation field is in the maximum amplitude.

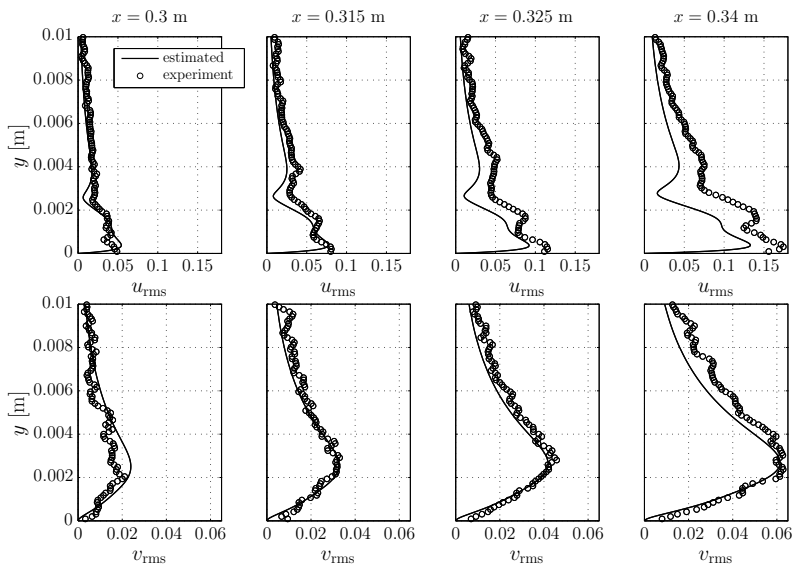


Figure 8: The estimated and measured rms value of the streamwise and wall-normal velocity components at four different streamwise locations.

The estimates deteriorate further downstream from the measurement sensor due to model uncertainties and nonlinearities. Note that the rms of the perturbation grows with a factor 3 between within $0.3 \text{ m} \leq x \leq 0.34 \text{ m}$. The distorted structure for the measured streamwise perturbation in the downstream region also indicates the presence of spanwise wavelengths induced by the nonlinearities. Additionally, uncertainties in the base flow and Reynolds number give rise to uncertainties in the wavespeed, spatial wavelength and growth rate which accumulate downstream from the sensor. Therefore to achieve a good robustness to these uncertainties the actuator is placed close to the feedforward sensor.

To the best of our knowledge, this is the first time that model-based estimates of the perturbation field are matched with experimental data. The results indicate that model-based control theory, that makes a-priori assumptions on the external disturbances, is able to predict the linear dynamics of natural flow perturbations.

3.2. Controller

The state feedback is designed to minimise the fluctuating wall-shear stress defined by $q = \int h(x)(\partial u / \partial y) dx$ where $h(x)$ is a Gaussian function centred at $x_q = 0.38$ with a width of 1 cm. The actuator is modelled as a linearly distributed body force with \mathcal{B}_2 the spatial distribution which is shown in figure 9. It describes how the unsteady modulation ϕ of the voltage signal $V_{\text{app}} = 0.5(V_0 + \phi) \sin(2\pi f_{\text{act}} t)$ is distributed in the domain. The body force is obtained by fitting a linear model through experimentally derived body force distributions obtained by Kotsonis & Ghaemi (2011), with the assumption that the body force is zero at the minimum discharge threshold of 6 kV_{pp} . It is assumed that the distribution gives a sufficient representation of the actual actuator, but the magnitude of the body force is assumed to be uncertain. The properties depend highly on the manufacturing process and the dielectric degrades over time resulting in an increased power consumption (Hanson *et al.* 2014). To make the control design tractable, an online tuning gain k is included to account for magnitude uncertainties in the body force model.

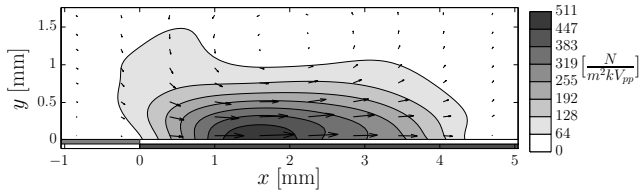


Figure 9: The modelled spatial distribution of the plasma actuator used for controller design.

This tuning gain scales the magnitude of the body force, or more convenient for control design, scales the magnitude of the control input $(1/k)\mathcal{B}_2\phi = \mathcal{B}_2\tilde{\phi}$. The controller is optimized for $\tilde{\phi}$ based on the nominal model and is multiplied with the tuning gain $\phi = k\tilde{\phi}$ when applied in real-time. The voltage signal to the actuator is thus given by $V_{\text{app}} = 0.5(V_0 + k\tilde{\phi}) \sin(2\pi f_{\text{act}}t)$ where $\tilde{\phi}$ is supplied by the compensator. Note that this tuning is consistent with the optimal control design since this change of coordinate not only scales the magnitude of \mathcal{B}_2 , but also changes the control penalty in the well known LQR control objective

$$\mathcal{J} = \lim_{T \rightarrow \infty} \frac{1}{T} \int_0^T q^2 + \left(\frac{l}{k}\phi\right)^2 dt, = \lim_{T \rightarrow \infty} \frac{1}{T} \int_0^T q^2 + (l\tilde{\phi})^2 dt \quad (3.4)$$

that is minimized by the controller. The control penalty l is tuned such that the complete compensator reduces the energy q^2 with two orders of magnitude for the nominal case $k = 1$. It is rather aggressively tuned, but it can be easily detuned online to not aggravate the flow.

To study the maximum attainable performance that can be achieved by the compensator, offline simulations have been performed in which the linearised equations are forced with a uniform stochastic disturbance. The spatial distribution of the disturbance is modelled as divergence free Gaussian distribution placed upstream of the control domain (Bagheri *et al.* 2009). The base flow distortion introduced by the average constant forcing of the plasma actuator is taken into account in the computation of the base flow used for the linear simulations. Note that the control model is based on the nominal undistorted base flow which introduces a difference between modelled flow and the simulated flow (and experimental flow in the next section). Figure 10 shows the wall-normal maximum amplitude of the rms streamwise velocity without control, with continuous forcing at 8 kV_{pp} and 9 kV_{pp}, and with LQG control at these two offset voltages. The spatial growth of the uncontrolled perturbation in the control domain is accordance with growth observed in figure 8. The constant forcing has a significant stabilizing effect on the flow which accumulates over distance from the location of the actuator due to the generated streamwise jet. The significant stabilization can also be contributed to the low Reynolds number and the high pressure gradient of the flow. The added momentum modifies the base flow, such that the resulting profile is less likely to develop an inflection point locally thereby improving the local stability properties. Nonetheless, the LQG controller achieves an additional one order of magnitude reduction as compared to continuous forcing both for the 8 kV_{pp} and 9 kV_{pp} offset case.

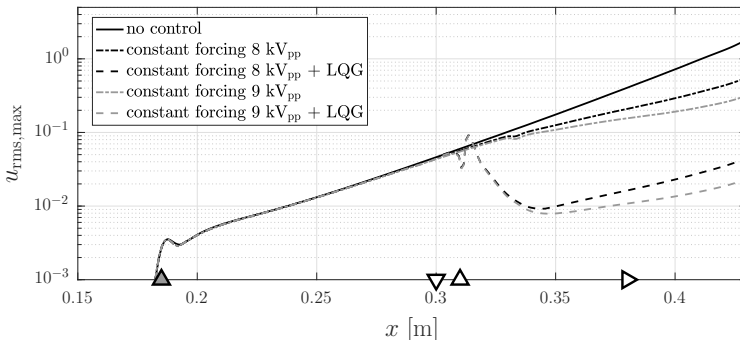


Figure 10: Offline simulation of a uniform white disturbance. Shown is the wall-normal maximum of the rms streamwise velocity. The triangles indicate the location the disturbance source (dark \triangle), the sensor (∇), the actuator (\triangle) and the control objective (\triangleright).

4. Experimental control performance

In this section the nominal performance and the robust performance in off-design conditions of the compensator is evaluated. All results contain a comparison between an 8 kV_{pp} and a 9 kV_{pp} mean voltage supply. The performance of the compensator is in particular compared against the performance with open-loop continuous forcing to properly evaluate the contribution of the unsteady actuation. The control objective is evaluated based on the downstream microphone signal p_2 which is recorded for periods of 20 s sampled at 30 kHz. Evaluation of the time domain performance is based on the standard deviation of the signal. To compute the standard deviation, the signal is filtered between 50-800 Hz to filter out the low frequency background noise (see also figure 4(b)) and the high frequency noise at 2 kHz of the plasma actuator. It was found that the actuator was stronger than assumed in the control design. Additionally it was observed that strong actuation can in fact promote transition due to nonlinear effects and control spillover (Balas 1978), which should be avoided. Therefore the controller had to be detuned to achieve an effective stabilisation. For the nominal designed case, the data was recorder for $k \in [0.25 \ 0.5]$ with steps of $\Delta k = 0.05$. The effect of the tuning gain on the standard deviation for the nominal designed case is shown in figure 11. With the proper tuning, a reduction of 50-55% in standard deviation compared to open-loop forcing has been measured. The effect of the tuning gain is best observed in the frequency domain. Figure 12 compares the power spectral density for the 8 kV_{pp}, $k = (0.35, 0.5)$ control cases (Figure 12(a)) and for the 9 kV_{pp}, $k = (0.3, 0.4)$ control cases (Figure 12(b)). At these values the effect of the tuning gain was best observed. A higher gain might give a better attenuation of the most amplified frequencies, but in turn results in more spillover at the lower frequencies.

For example for the 9 kV_{pp}, $k = 0.4$ control case the energy at most amplified frequencies is reduced with two orders of magnitude (40 dB), while the $k = 0.3$ controller reduces the peak with 20 dB. Nevertheless, the standard deviation at $k = 0.4$ is higher as the amplitude at the spillover frequencies ($f < 130$ Hz) dominate the stabilised bandwidth. A similar observation can be made for the 8 kV_{pp} control cases. However, the effect is more pronounced for the 9 kV_{pp} cases as it achieves a better open-loop stabilisation of the most amplified frequencies. The 8 kV_{pp} open-loop forcing gives a reduction of $1 - \sigma_{ol}/\sigma_{unc} = 65\%$, whereas the 9 kV_{pp} open-loop forcing gives an 88%

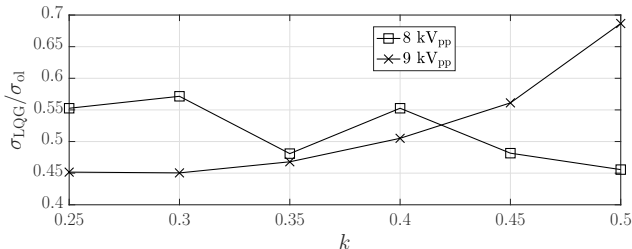


Figure 11: Effect of the online tuning gain on the standard deviation of the downstream sensor signal. Shown is the ratio between the LQG controlled case and the open-loop forcing case. ($\sigma_{unc} = 1.987$, $\sigma_{ol}^{8kV_{pp}} = 0.766$, $\sigma_{ol}^{9kV_{pp}} = 0.239$.)

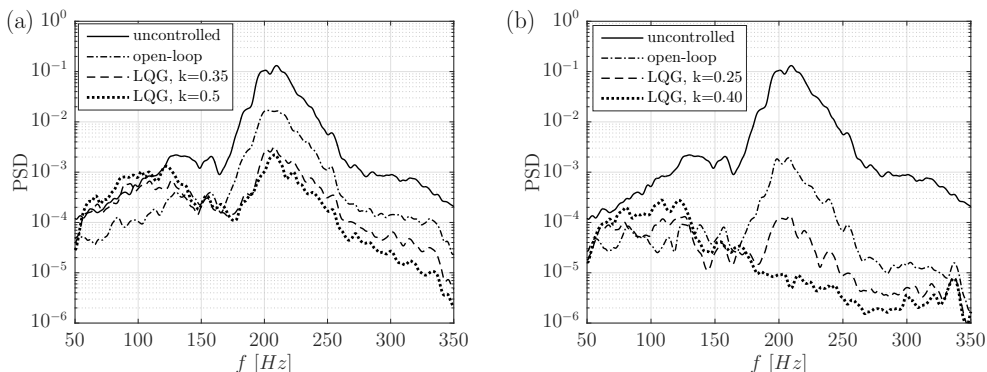


Figure 12: Power spectral density of the downstream sensor signal without control, with open-loop control and LQG control. (a) 8 kV_{pp} mean voltage supply. (b) 9 kV_{pp} mean voltage supply.

reduction. This significant stabilisation can also be contributed to the low free-stream velocity as discussed in the previous section. In fact, 9 kV_{pp} open-loop forcing gives a better performance than the 8 kV_{pp} LQG control performance. Therefore the main benefit for the investigated conditions is a reduced power compensation. However, at higher freestream velocities, the jet added by the plasma actuators decreases and open-loop control becomes less effective, see also figure 13.

Figure 13 shows the effect of the wind-tunnel speed on the standard deviation for $k = 0.35$. and the PSD at two off-design windtunnel speeds is shown in figure 14. Variations in the freestream velocity from the design condition at $U_\infty = 9.4$ m/s give a reduced performance. Nevertheless, the controller provides a reduction as compared to open-loop forcing in particular in the higher range of freestream velocities. The controller is still able to significantly reduce the spectral density at most amplified frequencies in off-design conditions. However, at lower free-stream velocities the spillover becomes more dominant as can be seen from 14, resulting a reduced effectiveness. In short, the most amplified frequencies are successfully reduced by compensator. However, the effectiveness as compared to open-loop forcing is reduced as the mean applied forcing already provides a significant stabilisation. As a result the spillover at lower frequencies introduced by the unsteady actuation becomes more dominant. Nevertheless, the compensator is able to achieve a robust reduction in standard deviation between 30-60% within the range 8.4-

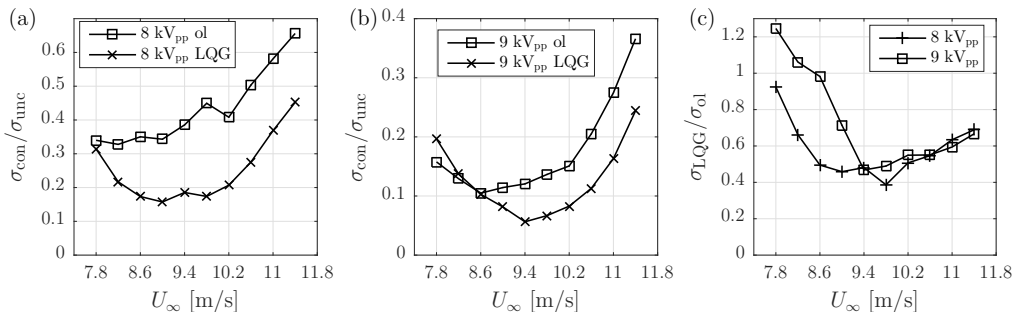


Figure 13: Effect of wind-tunnel speed variation on the standard deviation of the downstream sensor signal ($k = 0.35$). Ratio between the controlled (LQG and open-loop) and the uncontrolled case with 8 kV_{pp} mean supply (a) and 9 kV_{pp} mean supply (b). (c) Ratio between the LQG controlled and open-loop forcing case.

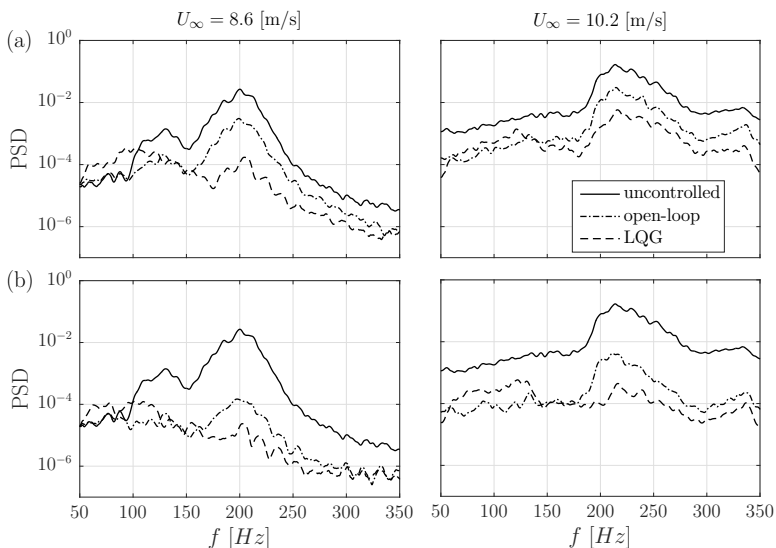


Figure 14: Power spectral density of the downstream sensor signal at two off-design freestream velocities. (a) 8 kV_{pp} mean supply. (b) 9 kV_{pp} mean supply.

11.4 m/s as compared to open-loop forcing. It is expected that the relative effectiveness will improve at higher freestream velocities, where unsteady forcing is the only option to achieve stabilisation of the flow.

5. Discussion and conclusion

For the first time, an experimental implementation of a physics model-based compensator strategy has been applied in a natural TS-wave dominated flow over a flat plate. Such white-box methods are not yet considered competitive in an applied setting due to their difficulty in obtaining an accurate representation of the upstream disturbance environment. However, it is experimentally verified that the Kalman filter, which makes a priori assumptions on the noise characteristics, is able to predict the effect of upstream

disturbances and to estimate TS-waves naturally occurring in a low freestream turbulence environment. This leads to the following conclusions: (1) it is the effect of upstream disturbances that is important to model and not the disturbances itself (which is more complex than assumed) and (2) the effect of external disturbances can be properly modelled by an inflow disturbance model.

A single DBD plasma actuator is used to simultaneously increase the local stability of the boundary layer and to attenuate the TS-waves through unsteady modulation of the actuator voltage signal. The performance and robustness of the controller is compared to the case of continuous actuation. Results show that the controller is able to additionally reduce the spectral density at the most amplified frequencies with more than one order of magnitude and is capable of reducing the standard deviation of the unsteady pressure signal between 30-60% for a range of off-design freestream velocities, measured 9 cm downstream from the actuator. While this reduction is less than theoretically can be achieved in numerical simulations, it is of the same order as what has been achieved in recent experimental studies using system identification techniques. To the best of our knowledge, the best performance was reported by Goldin *et al.* (2013), who achieved a maximum localised reduction of 85% of the downstream sensor signal in a natural TS-wave dominated boundary layer flow. Juillet *et al.* (2014) achieved an average localised reduction of 45% in a convective dominated channel flow and Gautier & Aider (2014) achieved a 35% reduction in turbulent kinetic energy fluctuations in a convective backward-facing step flow. It should be noted that the maximum attainable performance also depends on the choice of the actuator/sensor setup and the disturbance scenario (TS-dominated, streak dominated, intensity, amplitude, etc.). Furthermore, the spatial extent of the reduction should be contrasted to length scales of the perturbations and the placement of the objective sensor. A similar experimental setup and white-box approach was considered by Fabbiane *et al.* (2015) to suppress TS-waves in a boundary layer flow using a single plasma actuator, but introduced the upstream disturbances artificially. For uniform (white) disturbances they achieved a maximum reduction in standard deviation of 60%, compared to the uncontrolled case, measured 5 cm downstream of the actuator.

Fabbiane *et al.* (2015) also stressed the robustness issues of disturbance feedforward optimal controllers for transition delay. The framework used in this study also shows promise for the development of robust feedback controllers to guarantee both robust stability and robust performance in off-design conditions, e.g. using \mathcal{H}_∞ and μ -synthesis techniques. It was shown in (Belson *et al.* 2013) that in case of feedback actuator/sensor configurations, the sensor has to be placed close behind the actuator (less than one wave-length of the perturbations) and that such configurations are highly sensitive to neglected/truncated dynamics resulting from the model reduction step. By synthesizing the reduced-order compensator directly from the governing equation, avoids both the need for data-driven empirical model reduction and system-identification, allowing for an accurate reduction of the dynamics also for feedback actuator/sensor configurations. In this study the sensor was also placed 1 cm in front of the actuator, which is less than half the wave-length of the most amplified perturbation, showing that the compensator can cope with the electromagnetic inference introduced by the actuator.

Based on the presented results it can be concluded that the linear control approach presented in this article is a competitive technique in an applied setting. It provides an efficient means to synthesise compensators directly from the governing equations without the use of prior numerical data or experimental data. It is able to estimate and control natural flow perturbations and provides a promising direction for control of convective instabilities in wall-bounded shear flows. The question whether the modelling/synthesis approach in this study is more viable than the empirical model reduction tools and

system-identification techniques currently available in the community should be carefully investigated in future works.

REFERENCES

- BAGHERI, S., BRANDT, L. & HENNINGSON, D. S. 2009 Input–output analysis, model reduction and control of the flat-plate boundary layer. *Journal of Fluid Mechanics* **620**, 263–298.
- BALAS, M. J. 1978 Feedback control of flexible systems. *IEEE Transactions on Automatic Control* **23** (4), 673–679.
- BELSON, B. A., SEMERARO, O., ROWLEY, C. W. & HENNINGSON, D. S. 2013 Feedback control of instabilities in the two-dimensional blasius boundary layer: The role of sensors and actuators. *Physics of Fluids (1994-present)* **25** (5), 054106.
- BEWLEY, T. R. & LIU, S. 1998 Optimal and robust control and estimation of linear paths to transition. *Journal of Fluid Mechanics* **365**, 305–349.
- DADFAR, R., SEMERARO, O., HANIFI, A. & HENNINGSON, D. S. 2013 Output feedback control of blasius flow with leading edge using plasma actuator. *AIAA journal* **51** (9), 2192–2207.
- FABBIANE, N., SIMON, B., FISCHER, F., GRUNDMANN, S., BAGHERI, S. & HENNINGSON, D. S. 2015 On the role of adaptivity for robust laminar flow control. *Journal of Fluid Mechanics* **767**, R1.
- GAUTIER, N. & AIDER, J.-L. 2014 Feed-forward control of a perturbed backward-facing step flow. *Journal of Fluid Mechanics* **759**, 181–196.
- GOLDIN, NIKOLAS, KING, RUDIBERT, PÄTZOLD, ANDREAS, NITSCHKE, WOLFGANG, HALLER, DANIEL & WOIAS, PETER 2013 Laminar flow control with distributed surface actuation: damping tollmien-schlichting waves with active surface displacement. *Experiments in Fluids* **54** (3), 1–11.
- HANSON, RONALD E, HOUSER, NICOLE M & LAVOIE, PHILIPPE 2014 Dielectric material degradation monitoring of dielectric barrier discharge plasma actuators. *Journal of Applied Physics* **115** (4), 043301.
- HERVÉ, A., SIPP, D., SCHMID, P. J. & SAMUELIDES, M. 2012 A physics-based approach to flow control using system identification. *Journal of Fluid Mechanics* **702**, 2658.
- JUILLET, F., MCKEON, B. J. & SCHMID, P. J. 2014 Experimental control of natural perturbations in channel flow. *Journal of Fluid Mechanics* **752**, 296–309.
- KOTSONIS, M. & GHAEMI, S. 2011 Forcing mechanisms of dielectric barrier discharge plasma actuators at carrier frequency of 625 hz. *Journal of Applied Physics* **110** (11), 113301.
- KURZ, A., GOLDIN, N., KING, R., TROPEA, C. & GRUNDMANN, S. 2013 Hybrid transition control approach for plasma actuators. *Experiments in fluids* **54** (11), 1610.
- LAI, M. J. & SCHUMAKER, L. L. 2007 *Spline functions on triangulations*. Cambridge University Press.
- MOORE, B. C. 1981 Principal component analysis in linear systems: Controllability, observability, and model reduction. *IEEE Transactions on Automatic Control* **26** (1), 17–32.
- ROWLEY, C. W. & DAWSON, S. T. M 2017 Model reduction for flow analysis and control. *Annual Review of Fluid Mechanics* **49**, 387–417.
- SIPP, D. & SCHMID, P. J. 2016 Linear closed-loop control of fluid instabilities and noise-induced perturbations: A review of approaches and tools. *Applied Mechanics Reviews* **68** (2), 020801.
- TOL, H. J., KOTSONIS, M. & DE VISSER, C. C. 2018 Pressure based estimation and control of ts-waves in falkner-skann boundary layers. *under review in AIAA journal* **xx**, xx.
- TOL, H. J., KOTSONIS, M., DE VISSER, C. C. & BAMIEH, B. 2017 Localised estimation and control of linear instabilities in two-dimensional wall-bounded shear flows. *Journal of Fluid Mechanics* **824**, 818–865.
- TOL, H. J., DE VISSER, C. C. & KOTSONIS, M. 2016 Model reduction of parabolic PDEs using multivariate splines. *International Journal of Control* **0**, 1–16.
- VAN INGEN, JL 2008 The e^n method for transition prediction: Historical review of work at tu delft. In *Proceedings of the 38th AIAA Fluid Dynamics Conference and Exhibit*. AIAA.
- ZHOU, K., DOYLE, J. C. & GLOVER, K. 1996 *Robust and optimal control*, , vol. 40. Prentice hall New Jersey.